



1 Quantification of toxic metallic elements using machine 2 learning techniques and spark emission spectroscopy

3 Seyyed Ali Davari^{1,2,*} and Anthony S. Wexler^{1,2}

4 ¹Air Quality Research Center (AQRC), University of California, Davis, 95616, Davis, USA

5 ²Department of Mechanical and Aerospace Engineering, Civil and Environmental
6 Engineering, and Land, Air and Water Resources, University of California, Davis, USA

7 Abstract

8 The United States Environmental Protection Agency (US EPA) list of Hazardous Air Pollutants
9 (HAPs) includes metal elements suspected or associated with development of cancer. Traditional tech-
10 niques for detecting and quantifying toxic metallic elements in the atmosphere are either not real time,
11 hindering identification of sources, or limited by instrument costs. Spark emission spectroscopy is a
12 promising and cost effective technique that can be used for analyzing toxic metallic elements in real
13 time. Here, we have developed a cost-effective spark emission spectroscopy system to quantify the con-
14 centration of toxic metallic elements targeted by US EPA. Specifically, Cr, Cu, Ni, and Pb solutions were
15 diluted and deposited on the ground electrode of the spark emission system. Least Absolute Shrinkage
16 and Selection Operator (LASSO) was optimized and employed to detect useful features from the spark-
17 generated plasma emissions. The optimized model was able to detect atomic emission lines along with
18 other features to build a regression model that predicts the concentration of toxic metallic elements from
19 the observed spectra. The limits of detections (LOD) were estimated using the detected features and
20 compared to the traditional single-feature approach. LASSO is capable of detecting highly sensitive fea-
21 tures in the input spectrum; however for some elements the single-feature LOD marginally outperforms
22 LASSO LOD. The combination of low cost instruments with advanced machine learning techniques for
23 data analysis could pave the path forward for data driven solutions to costly measurements.



24 1 Introduction

25 The United States Environmental Protection Agency (US EPA) lists a number of metals in their list of
26 Hazardous Air Pollutants (HAPs). These metals are known or suspected to cause cancer or other serious
health effect Buzea et al. (2007); Pope III et al. (2002). Table 1 lists the metals in US EPA's HAPs list. Table

Table 1: List of hazardous metallic elements targeted by US EPA

US EPA Metal HAPS
Antimony
Arsenic
Beryllium
Cadmium
Chromium
Cobalt
Lead
Manganese
Mercury
Nickel
Selenium

27
28 2 lists other metals that are not on US EPA's HAPs list but have been implicated in a range of adverse health
effects so are of concern to the California Air Resources Board (CARB). X-ray fluorescence (XRF) Van Meel

Table 2: List of other toxic metals

Metallic Element
Cr
Cu
Ni
Pb

29
30 et al. (2007); Vincze et al. (2002) and inductively coupled plasma mass spectrometry (ICP-MS) Rovelli
31 et al. (2018); Venccek et al. (2016) have been used traditionally to quantify metals in atmospheric particles.
32 XRF is excellent for measuring lighter elements and metals on filter substrates, but for field application it
33 is expensive, has a high LOD for heavier elements, and includes radiation risk. ICP-MS requires collection
34 of aerosol on a substrate, such as a filter or impactor foil, extraction of the metals or elements from the
35 substrate using harsh acidic chemicals, and then analyzing in the ICP-MS along with standards that help
36 the instrument quantitate. Moreover, ICP-MS is most suitable for heavier elements and metals so has a high
37 LOD for lighter toxic metals and is not available in field-deployed, real-time applications. Spark-induced
38 breakdown spectroscopy (SIBS) and laser-induced breakdown spectroscopy (LIBS) have been employed in
39 various applications from combustion Do and Carter (2013); Kiefer et al. (2012); Kotzagianni et al. (2016),
40 nanomaterials Davari et al. (2017a); De Giacomo et al. (2011); Hu et al. (2017); Matsumoto et al. (2015a,b,
41 2016), and environmental/bio-hazards Diwakar et al. (2012); Diwakar and Kulkarni (2012); Zheng et al.
42 (2018), forensics Martin et al. (2007), semiconductors and thin films Axente et al. (2014); Davari et al.
43 (2017b, 2019); Hermann et al. (2019), explosives Gottfried et al. (2009), pharmaceuticals Mukherjee and
44 Cheng (2008a,b); St-Onge et al. (2002), and biomedical Abbasi et al. (2018); Baudelet et al. (2006); Davari
45 et al. (2018). Particularly, Fisher et al. Fisher et al. (2001) studied various toxic metals in aerosols by
46 optimizing the spectrometer response with respect to gate delay. Hunter et al. employed spark emission
47 spectroscopy for continuous monitoring of metallic elements in aerosols Hunter et al. (2000). Yao et al.
48 used spark emission spectroscopy to obtain the carbon content of fly ashes Yao et al. (2018). Diwakar
49 et al. Diwakar and Kulkarni (2012) employed spark emission spectroscopy coupled with a corona aerosol
50 microconcentrator (CAM) to improve the particle collection efficiency and detection limits of toxic metallic
51 elements. Zheng et al. Zheng et al. (2017) characterized the CAM performance with respect to different



52 experimental parameters and obtained the optimized design parameters for their CAM system. In this study,
53 we employed spark emission spectroscopy to quantify toxic metallic elements. We also developed low-cost
54 components to substantially reduce the cost of the system. The resulting instrument was evaluated against
55 four toxic metallic elements listed by US EPA and analyzed using advanced machine-learning techniques.

56 2 Instrument development:

57 2.1 Spark generation system:

58 One costly component that is required for developing a spark emission spectroscopy system is the spark
59 generation system. Numerous papers have studied the fundamental principles of spark emission spectroscopy
60 Sacks and Walters (1970); Walters (1969, 1977). The key idea is to discharge a capacitor as quickly as possible
61 to increase the power dissipated in the spark gap. Fig. 1 illustrates the schematic of the spark generation
system. The overall goal is to charge a capacitor at high voltage and once it has been charged sufficiently,

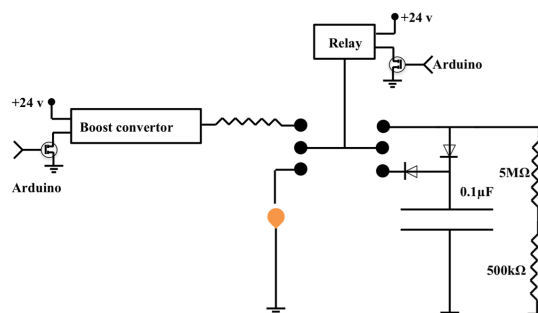


Figure 1: Schematic of the built-in spark generation system.

62 discharge the capacitor through the spark gap. An Arduino board controls the timing between charging and
63 discharging the capacitor. A boost converter converts 24v DC to 5000v DC and is connected to a mechanical
64 relay with two switching states controlled with the Arduino board. In the charge state, the mechanical relay
65 provides the conduction path between the boost converter and the capacitor. In this configuration, the
66 capacitor reaches full charge in $5\mu\text{s}$. Once the capacitor is fully charged, the Arduino board sends a signal

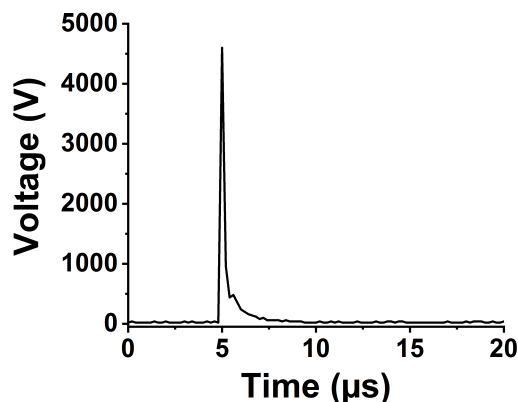


Figure 2: Spark voltage evolution in time.



68 to turn off the boost convertor and sends another signal to the mechanical relay to flip to the discharge
69 state. At the discharge state, the mechanical relay provides a conduction path between the capacitor and
70 the spark gap. Previous studies Shepherd et al. (2000) showed that the discharge process could be controlled
71 by a resistor after the spark gap. For low resistor values, the spark current exhibited a periodic behavior as
72 the capacitor discharges, which can be associated with an under damped discharging. On the other hand,
73 increasing the resistor value damped the discharge process and dissipated a large portion of the capacitor
74 energy through the resistor instead of the spark gap. In our setup, a 10Ω resistor maximizing power dissipation
75 in the spark gap, while minimizing oscillations. Fig. 2 illustrates the evolution of the generated spark as a
76 function of time. The voltage shows a sudden increase followed by an exponential decrease fully discharging
77 in less than 5s and thus delivering sufficient energy to the arc and deposited analyte.

78 2.2 Delay generator:

79 The delay generator is another costly component typically used in time-resolved spectroscopy. Electronics
80 advances have paved the way for developing a cost-effective delay generator. The delay generator suppresses
81 initial noise in the emission spectrum so needs to cover a range between $1\mu\text{s}$ and $20\mu\text{s}$ with resolution less
82 than $0.2\mu\text{s}$. We designed a custom-built delay generator in order to lower the overall cost of the instrument.
83 Fig. 3 illustrates the schematic of the circuit. Upon generation of the spark-induced plasma, a pair of

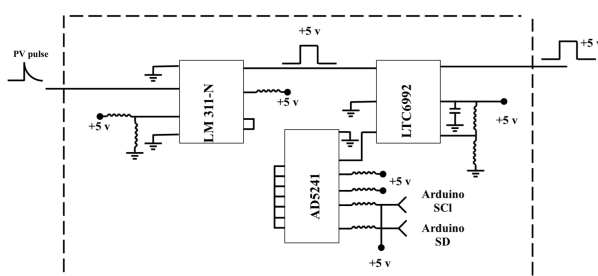


Figure 3: Schematic of the built-in delay generator.

83 lenses collect and focus the plasma emission into a photodiode. The pulse generated by the photodiode
84 is passed into a voltage comparator (LM 311-N) to generate a transistor–transistor logic (TTL) signal. The
85 output TTL signal from the comparator is sent to a pulse width modulator (PWM) controller (LTC6992),
86 which adds delay to the TTL signal. An Arduino board adjusts a digital resistor (AD5241), which in
87 turn determines the delay value. Fig. 4 shows that the observed and desired delays show a near one-to-
88 one relationship especially for short delay values. Considering the spark generated plasma short lifetime,
89 our measurements require short delay values ($< 5\mu\text{s}$) where the built-in delay generator shows excellent
90 performance and accuracy.

92 2.3 Spectra Collection:

93 Four toxic metallic elements with different concentrations were used to test the developed spark emission
94 spectrometer system performance. Cr, Cu, Ni and Pd ($1000\mu\text{g}/\text{mL}$) were purchased from AccuStandard and
95 diluted to specific concentrations. A micropipette was used to deposit diluted solutions on a 1 mm diameter
96 tungsten ground electrode of the spark system for emission analysis. Upon evaporation of the droplets, the
97 capacitor was discharged to ablate the deposited material and obtain spectra. A pair of lenses (75mm focal
98 length and 1" diameter, Thorlab) focused the emission into an optical fiber connected to a spectrometer
99 (Ocean Optics).

100 3 Results and discussions:

101 To address shot-to-shot variations in the spark-generated plasma and nullify possible faults caused by the low
102 cost components, an unsupervised learning technique, K-Means clustering, classifies the collected spectra.

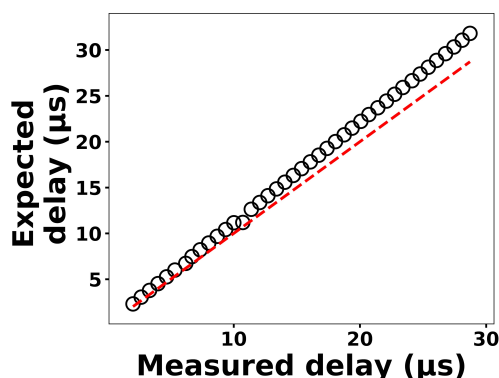


Figure 4: The expected delay set by the Arduino board as a function of the measured delay.

Following this procedure, it is possible to identify and remove outliers and hence improve the accuracy of

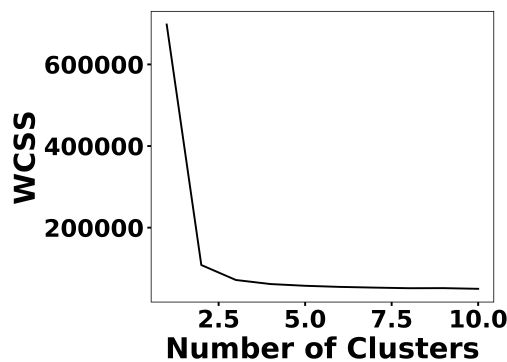


Figure 5: The elbow plot suggests two centroids for clustering the spectra set.

103
104 the analysis. Fig. 5 illustrates the elbow plot that is used to optimize the number of spectral classes. The
105 within-cluster sum of squares (WCSS) error plateaus once we have two or more centroids and therefore,
106 the number of centroids is set to two. Fig. 6 illustrates the performance of the model for 300 spectra
107 obtained from the background (tungsten ground electrode ablation). The results show clearly two clusters
108 with different emission response. The lower left cluster containing < 10% of the spectra represent low-
109 signal outliers so were eliminated from further analysis. For each element, 0.1, 1, 10 and 100 ng of mass
110 were deposited on the ground electrode. For each concentration, 10 spectra were collected using 2 μg delay
111 between the observed and recorded emissions. Feature scaling is a standard preprocessing step that improves
112 the model optimization process. Upon identifying and removing the outlier spectra, the cleaned spectra set
113 is normalized using the Tungsten peak at W I (400.87 nm) and fed into the Least Absolute Shrinkage and
114 Selection Operator (LASSO) algorithm for model development and prediction.

115 LASSO:

116 Simple linear regression obtains the slope and intercept of a linear line by minimizing the mean squared
117 error between the predictions and known values. Least absolute shrinkage and selection operator (LASSO)

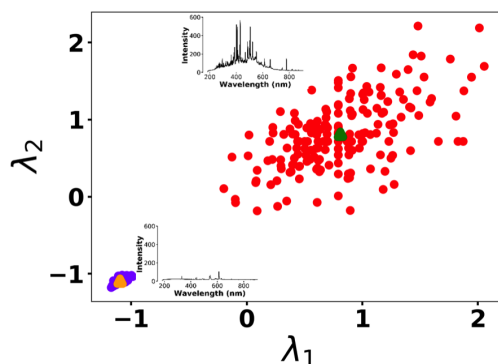


Figure 6: K-Means clustering for detecting outliers before passing the spectra set to LASSO model. Two clusters were plotted for the normalized intensities of two arbitrary wavelengths at λ_1 (208.365 nm) and λ_2 g (208.759 nm).

118 detects and employs more features to perform predictions by optimizing the following loss function:

$$J(\theta) = \frac{1}{m} \sum_{i=1}^m (y^{(i)} - h_{\theta}(\mathbf{x}^{(i)}))^2 + c \sum_{j=1}^k |\theta_j| \quad (1)$$

119 where $\mathbf{x}^{(i)} \in \mathbb{R}^{2048}$ and $h_{\theta}(\mathbf{x}^{(i)})$ represent the normalized spectrum and the model prediction for spectrum (i),
 120 respectively, where $y^{(i)}$ is the known concentration corresponding to spectrum (i). The LASSO coefficients
 121 are indicated by θ_j . The first term in equation (1) is the mean squared error and is common with simple
 linear regression, while the second term is a regularization term that minimizes the magnitude of θ_j . The

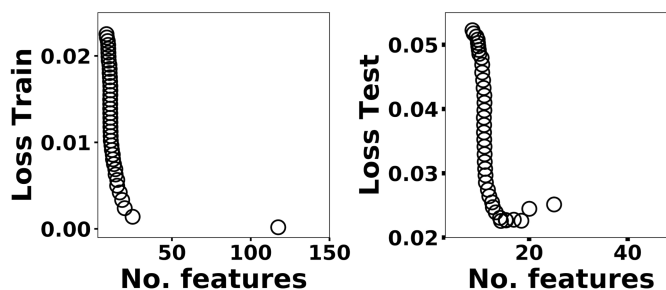


Figure 7: The train and test losses for Ni as a function of number of features.

122 L1 norm essentially sets most of the features in the spectrum to zero and maintains only a few features
 123 to build the linear model and perform predictions. The regularization constant (c) determines the number
 124 of features to be used in the model, and therefore the model loss needs to be optimized with respect to
 125 the regularization constant. To obtain the optimized regularization constant, we plotted the loss values for
 126 the Ni spectra training and testing sets as a function of number of features for various c values based on
 127 Leave-One-Out cross validation (Fig. 7). As expected, the train loss monotonically decreases as the number
 128 of features increases, while the loss for the test set initially decreases and then starts increasing. This implies
 129 that after incorporating a certain number of features into the model, the model starts memorizing rather
 130 than generalizing, which is known as overfitting. Therefore, we set the regularization constant to the value
 131 that minimizes the loss for the test set. Fig. 8 illustrates the optimized LASSO model predictions obtained
 132 by cross validation. For each concentration, the cross validation predictions were averaged and plotted along
 133

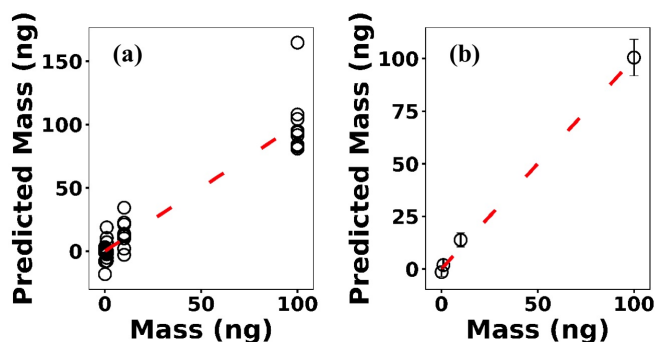


Figure 8: (a) LASSO predictions based on Leave-One-Out cross validation for Ni, (b) the averaged predictions for each concentration.

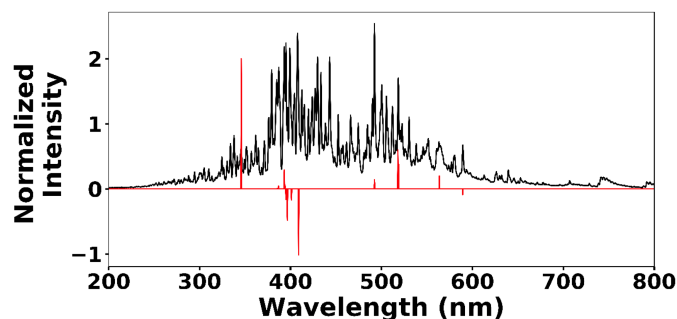


Figure 9: Ni 10ng spectrum (black line) and selected features by LASSO (red line).

134 with the standard deviations. The predicted values vary linearly with the actuals. Figure 9 shows the
 135 wavelengths chosen by LASSO and the mean spectrum for 10 ng. LASSO chose a few Ni emission peaks
 136 along with other features to build the model. The same optimization process was applied to other metallic
 137 elements specifically Cr, Cu, and Pb. Fig. 10 illustrates the resulting predictions and demonstrates the
 138 value of LASSO for predicting deposited mass from the spectra. To obtain the limit of detection (LOD), the
 139 following function of the LASSO coefficients θ_j was used:

$$LOD = 3 \frac{\sigma_B}{S} = 3\sigma_B \|\theta_B\| \quad (2)$$

140 where σ_B is the standard deviation of the background and $\|\theta_B\|$ is the Euclidean norm of LASSO coefficients.
 141 Table 3 reports the LODs of the studied metallic elements.

Multivariate regression models such as LASSO might be more powerful in detection and quantification

Table 3: Detection limits for various elements based on the LASSO and univariate models.

Element	LASSO	R^2	MAE_{LASSO}	Univariate	R^2	$MAE_{Univariate}$
Cr	3.55	0.99	6.71	3.28	0.98	3.83
Cu	12.09	0.92	49.67	0.68	0.11	143.27
Ni	9.60	0.98	6.67	2.32	0.88	68.63
Pb	54.40	0.90	36.67	8.37	0.45	124.42

142
 143 over univariate models; however, there is no guarantee that multivariate models outperform simple linear

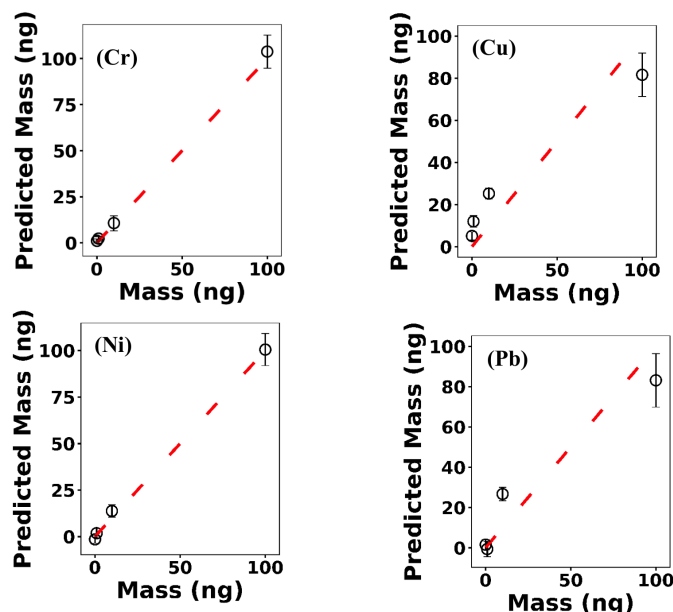


Figure 10: The optimized LASSO models predictions for Cr, Cu, Ni and Pb.

144 regression Braga et al. (2010); Castro and Pereira-Filho (2016). To compare LASSO to univariate methods,
 145 we calculated the LODs using simple univariate linear regression based on the features selected by LASSO.
 Fig. 11 illustrates the LODs obtained using this univariate technique (circles) compared to LASSO LOD

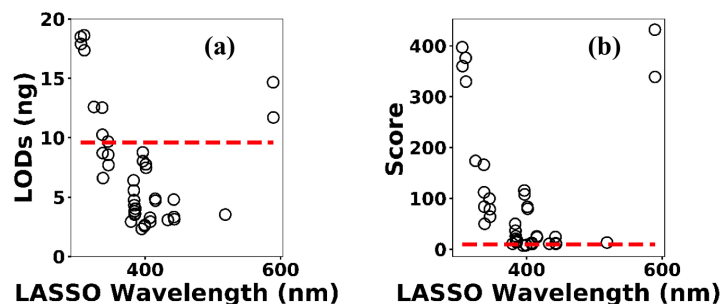


Figure 11: (a) the univariate LODs based on LASSO selected features and (b) LASSO and univariate models scores.

146 (dashed line) for Ni. Considering only the sensitivity (LOD) is necessary but not sufficient for evaluating
 147 model performance since low R^2 values are also problematic. Therefore, in order to incorporate both R^2 and
 148 LOD for model assessment, we defined a score as:
 149

$$Score = \left(\frac{LOD}{R^2}\right)^2 \quad (3)$$

150 Based on this definition, a model that has low LOD and high R^2 is desirable. LASSO score outperforms
 151 single feature linear regression for Pb, but the two methods were comparable for Cu, Ni, and Cr (Fig. 12).
 152 Other studies have reported that univariate techniques performed better than multivariate ones Braga et al.



153 (2010); Castro and Pereira-Filho (2016). In LASSO, this may be related to the cost function defined for the
154 regression (equation (1)). LASSO is a special case of elastic net family where both L1 and L2 norms are
155 combined and used in the cost function. Considering the cost function in equation (1), the model goal is
156 to minimize the prediction error and coefficient values (minimizing L1). This does not necessarily optimize
157 LOD. Therefore, cost function minimization does not correspond to LOD minimization. Considering Fig.
158 12, using features defined by LASSO in a univariate model may yield better LOD than that obtained by
159 LASSO alone. This might be an advantageous approach if the physical intuition of the features is not as
important as detection of toxic metallic elements.

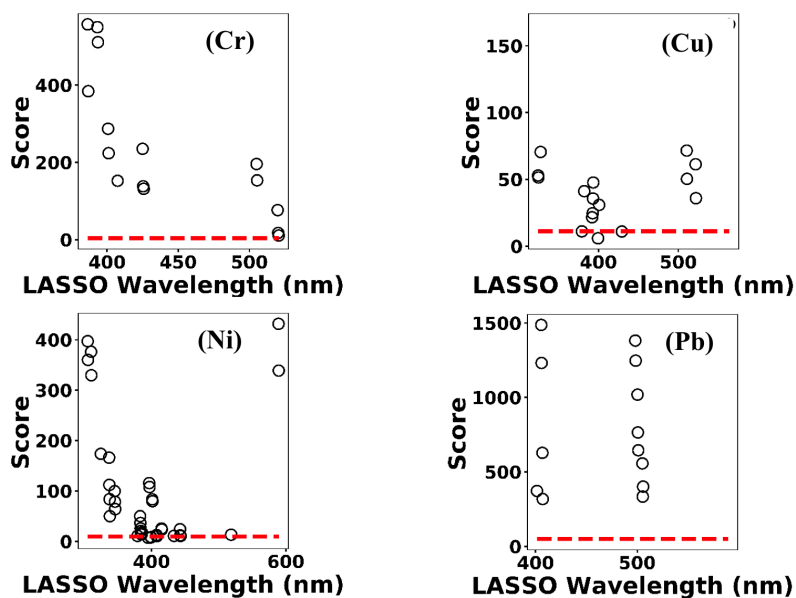


Figure 12: Model scores defined by equation 3 for Cr, Cu, Ni and Pb. Circles indicate univariate models scores and dashed lines correspond to LASSO scores.

160

161 4 Conclusion

162 A cost-effective spark emission spectroscopy instrument was designed and developed to quantify toxic metallic
163 elements targeted by US EPA and the California Air Resources Board. Costly components such as the spark
164 generation system and delay generator were developed to lower the overall cost. An unsupervised learning
165 technique was employed to detect outlier spectra. The cleaned spectra set was fed into LASSO for predicting
166 the concentration of deposited samples on the ground electrode of the spark system from spectra obtained
167 from the plasma. A combination of LASSO feature detection with univariate regression might improve the
168 detection limits. Our results illustrate the promising realm of cost-effective sensors combined with advanced
169 machine-learning techniques to provide data driven solutions to the traditional challenging problems.

170 Funding

171 California Air Resources Board (CARB).



¹⁷² **Disclosures**

¹⁷³ The authors declare no conflicts of interest.



174 References

- 175 Abbasi, H., Rauter, G., Guzman, R., Cattin, P. C., and Zam, A.: Laser-induced breakdown spectroscopy
176 as a potential tool for autcarbonization detection in laserosteotomy, *Journal of biomedical optics*, 23,
177 071 206, 2018.
- 178 Axente, E., Hermann, J., Socol, G., Mercadier, L., Beldjilali, S. A., Cirisan, M., Luculescu, C. R., Ristoscu,
179 C., Mihailescu, I. N., and Craciun, V.: Accurate analysis of indium–zinc oxide thin films via laser-induced
180 breakdown spectroscopy based on plasma modeling, *Journal of Analytical Atomic Spectrometry*, 29, 553–
181 564, 2014.
- 182 Baudalet, M., Guyon, L., Yu, J., Wolf, J.-P., Amodeo, T., Fréjafon, E., and Laloï, P.: Femtosecond time-
183 resolved laser-induced breakdown spectroscopy for detection and identification of bacteria: A comparison
184 to the nanosecond regime, *Journal of Applied Physics*, 99, 084 701, 2006.
- 185 Braga, J. W. B., Trevizan, L. C., Nunes, L. C., Rufini, I. A., Santos Jr, D., and Krug, F. J.: Comparison of
186 univariate and multivariate calibration for the determination of micronutrients in pellets of plant materials
187 by laser induced breakdown spectrometry, *Spectrochimica Acta Part B: Atomic Spectroscopy*, 65, 66–74,
188 2010.
- 189 Buzea, C., Pacheco, I. I., and Robbie, K.: Nanomaterials and nanoparticles: sources and toxicity, *Biointer-
190 phases*, 2, MR17–MR71, 2007.
- 191 Castro, J. P. and Pereira-Filho, E. R.: Twelve different types of data normalization for the proposition
192 of classification, univariate and multivariate regression models for the direct analyses of alloys by laser-
193 induced breakdown spectroscopy (LIBS), *Journal of Analytical Atomic Spectrometry*, 31, 2005–2014, 2016.
- 194 Davari, S. A., Hu, S., and Mukherjee, D.: Calibration-free quantitative analysis of elemental ratios in inter-
195 metallic nanoalloys and nanocomposites using Laser Induced Breakdown Spectroscopy (LIBS), *Talanta*,
196 164, 330–340, 2017a.
- 197 Davari, S. A., Hu, S., Pamu, R., and Mukherjee, D.: Calibration-free quantitative analysis of thin-film
198 oxide layers in semiconductors using laser induced breakdown spectroscopy (LIBS), *Journal of Analytical
199 Atomic Spectrometry*, 32, 1378–1387, 2017b.
- 200 Davari, S. A., Masjedi, S., Ferdous, Z., and Mukherjee, D.: In-vitro analysis of early calcification in aortic
201 valvular interstitial cells using Laser-Induced Breakdown Spectroscopy (LIBS), *Journal of biophotonics*,
202 11, e201600 288, 2018.
- 203 Davari, S. A., Taylor, P. A., Standley, R. W., and Mukherjee, D.: Detection of interstitial oxygen contents
204 in Czochralski grown silicon crystals using internal calibration in laser-induced breakdown spectroscopy
205 (LIBS), *Talanta*, 193, 192–198, 2019.
- 206 De Giacomo, A., De Bonis, A., Dell’Aglío, M., De Pascale, O., Gaudiuso, R., Orlando, S., Santagata, A.,
207 Senesi, G., Taccogna, F., and Teghil, R.: Laser ablation of graphite in water in a range of pressure from
208 1 to 146 atm using single and double pulse techniques for the production of carbon nanostructures, *The
209 Journal of Physical Chemistry C*, 115, 5123–5130, 2011.
- 210 Diwakar, P., Kulkarni, P., and Birch, M. E.: New approach for near-real-time measurement of elemental
211 composition of aerosol using laser-induced breakdown spectroscopy, *Aerosol Science and Technology*, 46,
212 316–332, 2012.
- 213 Diwakar, P. K. and Kulkarni, P.: Measurement of elemental concentration of aerosols using spark emission
214 spectroscopy, *Journal of analytical atomic spectrometry*, 27, 1101–1109, 2012.
- 215 Do, H. and Carter, C.: Hydrocarbon fuel concentration measurement in reacting flows using short-gated
216 emission spectra of laser induced plasma, *Combustion and Flame*, 160, 601–609, 2013.



- 217 Fisher, B. T., Johnsen, H. A., Buckley, S. G., and Hahn, D. W.: Temporal gating for the optimization of
218 laser-induced breakdown spectroscopy detection and analysis of toxic metals, *Applied Spectroscopy*, 55,
219 1312–1319, 2001.
- 220 Gottfried, J. L., De Lucia, F. C., Munson, C. A., and Miziolek, A. W.: Laser-induced breakdown spec-
221 troscopy for detection of explosives residues: a review of recent advances, challenges, and future prospects,
222 *Analytical and bioanalytical chemistry*, 395, 283–300, 2009.
- 223 Hermann, J., Axente, E., Pelascini, F., and Craciun, V.: Analysis of Multi-elemental Thin Films via
224 Calibration-Free Laser-Induced Breakdown Spectroscopy, *Analytical chemistry*, 91, 2544–2550, 2019.
- 225 Hu, S., Ribeiro, E. L., Davari, S. A., Tian, M., Mukherjee, D., and Khomami, B.: Hybrid nanocompos-
226 ites of nanostructured Co₃O₄ interfaced with reduced/nitrogen-doped graphene oxides for selective
227 improvements in electrocatalytic and/or supercapacitive properties, *Rsc Advances*, 7, 33 166–33 176, 2017.
- 228 Hunter, A. J., Morency, J. R., Senior, C. L., Davis, S. J., and Fraser, M. E.: Continuous emissions monitoring
229 using spark-induced breakdown spectroscopy, *Journal of the Air & Waste Management Association*, 50,
230 111–117, 2000.
- 231 Kiefer, J., Tröger, J. W., Li, Z., Seeger, T., Alden, M., and Leipertz, A.: Laser-induced breakdown flame
232 thermometry, *Combustion and flame*, 159, 3576–3582, 2012.
- 233 Kotzagianni, M., Yuan, R., Mastorakos, E., and Couris, S.: Laser-induced breakdown spectroscopy measure-
234 ments of mean mixture fraction in turbulent methane flames with a novel calibration scheme, *Combustion
235 and Flame*, 167, 72–85, 2016.
- 236 Martin, M. Z., Labbé, N., André, N., Harris, R., Ebinger, M., Wullschleger, S. D., and Vass, A. A.: High res-
237 olution applications of laser-induced breakdown spectroscopy for environmental and forensic applications,
238 *Spectrochimica Acta Part B: Atomic Spectroscopy*, 62, 1426–1432, 2007.
- 239 Matsumoto, A., Tamura, A., Honda, T., Hirota, T., Kobayashi, K., Katakura, S., Nishi, N., Amano, K.-i.,
240 Fukami, K., and Sakka, T.: Transfer of the species dissolved in a liquid into laser ablation plasma: an
241 approach using emission spectroscopy, *The Journal of Physical Chemistry C*, 119, 26 506–26 511, 2015a.
- 242 Matsumoto, A., Tamura, A., Koda, R., Fukami, K., Ogata, Y. H., Nishi, N., Thornton, B., and Sakka,
243 T.: On-site quantitative elemental analysis of metal ions in aqueous solutions by underwater laser-induced
244 breakdown spectroscopy combined with electrodeposition under controlled potential, *Analytical chemistry*,
245 87, 1655–1661, 2015b.
- 246 Matsumoto, A., Tamura, A., Koda, R., Fukami, K., Ogata, Y. H., Nishi, N., Thornton, B., and Sakka,
247 T.: A calibration-free approach for on-site multi-element analysis of metal ions in aqueous solutions by
248 electrodeposition-assisted underwater laser-induced breakdown spectroscopy, *Spectrochimica Acta Part B:
249 Atomic Spectroscopy*, 118, 45–55, 2016.
- 250 Mukherjee, D. and Cheng, M.-D.: Characterization of carbon-containing aerosolized drugs using laser-
251 induced breakdown spectroscopy, *Applied spectroscopy*, 62, 554–562, 2008a.
- 252 Mukherjee, D. and Cheng, M.-D.: Quantitative analysis of carbonaceous aerosols using laser-induced break-
253 down spectroscopy: a study on mass loading induced plasma matrix effects, *Journal of Analytical Atomic
254 Spectrometry*, 23, 119–128, 2008b.
- 255 Pope III, C. A., Burnett, R. T., Thun, M. J., Calle, E. E., Krewski, D., Ito, K., and Thurston, G. D.: Lung
256 cancer, cardiopulmonary mortality, and long-term exposure to fine particulate air pollution, *Jama*, 287,
257 1132–1141, 2002.
- 258 Rovelli, S., Nischkauer, W., Cavallo, D. M., and Limbeck, A.: Multi-element analysis of size-segregated fine
259 and ultrafine particulate via Laser Ablation-Inductively Coupled Plasma-Mass Spectrometry, *Analytica
260 chimica acta*, 1043, 11–19, 2018.



- 261 Sacks, R. D. and Walters, J. P.: Short-time, spatially-resolved radiation processes in a high-voltage spark
262 discharge, *Analytical Chemistry*, 42, 61–84, 1970.
- 263 Shepherd, J. E., Krok, J. C., and Lee, J. J.: Spark ignition energy measurements in Jet A, 2000.
- 264 St-Onge, L., Kwong, E., Sabsabi, M., and Vadas, E.: Quantitative analysis of pharmaceutical products by
265 laser-induced breakdown spectroscopy, *Spectrochimica Acta Part B: Atomic Spectroscopy*, 57, 1131–1140,
266 2002.
- 267 Van Meel, K., Smekens, A., Behets, M., Kazandjian, P., and Van Grieken, R.: Determination of platinum,
268 palladium, and rhodium in automotive catalysts using high-energy secondary target X-ray fluorescence
269 spectrometry, *Analytical chemistry*, 79, 6383–6389, 2007.
- 270 Venecek, M. A., Zhao, Y., Mojica, J., McDade, C. E., Green, P. G., Kleeman, M. J., and Wexler, A. S.:
271 Characterization of the 8-stage Rotating Drum Impactor under low concentration conditions, *Journal of*
272 *Aerosol Science*, 100, 140–154, 2016.
- 273 Vincze, L., Somogyi, A., Osan, J., Vekemans, B., Török, S., Janssens, K., and Adams, F.: Quantitative trace
274 element analysis of individual fly ash particles by means of X-ray microfluorescence, *Analytical chemistry*,
275 74, 1128–1135, 2002.
- 276 Walters, J.: Historical advances in spark emission spectroscopy, *Applied spectroscopy*, 23, 317–331, 1969.
- 277 Walters, J. P.: Spark discharge: Application multielement spectrochemical analysis, *Science*, 198, 787–797,
278 1977.
- 279 Yao, S., Xu, J., Zhang, L., Zhao, J., and Lu, Z.: Optimizing critical parameters for the directly measurement
280 of particle flow with PF-SIBS, *Scientific reports*, 8, 1868, 2018.
- 281 Zheng, L., Kulkarni, P., Zavvos, K., Liang, H., Birch, M. E., and Dionysiou, D. D.: Characterization of an
282 aerosol microconcentrator for analysis using microscale optical spectroscopies, *Journal of aerosol science*,
283 104, 66–78, 2017.
- 284 Zheng, L., Kulkarni, P., and Diwakar, P.: Spatial and temporal dynamics of a pulsed spark microplasma
285 used for aerosol analysis, *Spectrochimica Acta Part B: Atomic Spectroscopy*, 144, 55–62, 2018.